Microstructure characterization of high temperature mechanisms in a Nb–Ti–Si alloy

David Reyes, Virgil Malard, Stefan Drawin, Alain Couret, Jean-Philippe Monchoux

Microstructure characterization of high temperature mechanisms in a Nb-Ti-Si alloy

David Reyes[1], Virgil Malard[2], Stefan Drawin[2], Alain Couret[1], Jean-Philippe Monchoux[1*].

[1] CEMES, Université de Toulouse, CNRS, 29 rue Jeanne Marvig, BP 94347, 31055 Toulouse, France.

[2] ONERA-DMAS Université Paris Saclay, 29 Avenue de la Division Leclerc, BP 72, 92322 Châtillon Cedex, France

* To whom correspondence should be addressed: monchoux@cemes.fr (J.P. Monchoux).

Abstract

The deformation mechanisms of an Nb-20Si-25Ti-6Al-3Cr-3Mo alloy deformed in compression at 1000°C and at a strain rate of 10^{-4} s^{-1} have been investigated, using focused ion beam and transmission electron microscopy techniques. The initial microstructure of the alloy was constituted of a solid solution bcc Nb_{ss} matrix and of Nb_5Si_3 phases of β (tetragonal) and γ (hexagonal) crystallographic structures, with also hcp-Ti precipitates. As expected, the only phase which exhibited plastic deformation at 1000°C was the Nb_{ss} matrix. Glide of $\vec{b} = 1/2\langle 111 \rangle$ dislocations has been observed, in planes compatible with {112} and {123} planes, or with cross-slip in {110} planes, as classically reported in bcc structures. Conversely, climb contribution has not been evidenced, probably because of rearrangement of the climbing dislocations in sub-boundaries. Fine δ-$Nb_{11}Si_4$ precipitates have been detected in the samples compressed at 1000°C. Interactions of the δ-$Nb_{11}Si_4$ precipitates with the dislocations have been observed, which can potentially lead to strengthening of the Nb_{ss} phase.

Keywords: intermetallics (aluminides, silicides), powder metallurgy, dislocation structure, ion beam methods, transmission electron microscopy.

1. Introduction

Nb-silicides are good candidates as turbine blade materials in aero-engine devices, due to their high melting temperature compared to Ni-based superalloys [1, 2]. These materials exhibit a composite microstructure, with a matrix made of a Nb_{ss} solid solution, and zones constituted of intermetallic phases, like the α-, β- and γ-Nb_5Si_3 or Nb_3Si phases [1, 3] (the notation Nb_xSi_y

Accepted for publication in *Intermetallics* on 16/02/2022. DOI: 10.1016/j.intermet.2022.107509

is used even if alloying elements like Ti, Mo, Cr… substitute for Nb and Al, Ge… for Si). Most of the time, Ti is a major constituent, and the microstructures are described in the framework of the ternary Nb-Ti-Si phase diagram [4-8]. Many efforts have been undertaken to improve the properties of these materials by alloying them with several elements (Cr, Hf, Y, Al, B…), notably to address the question of the resistance to oxidation, which remains problematic [9-12]; depending on the nature and content of these alloying elements, more intermetallic phases can appear, like $NbCr_2$ and Nb_5Si_2B. Numerous works have concentrated on the mechanical properties of various Nb-silicides [1, 9, 10, 13, 14]. These studies showed that the Nb_5Si_3 phase exhibits a marked brittle behavior, whereas the Nb_{ss} matrix provides ductility and toughness to the material [1, 13]. It was shown also that the Nb_{ss} phase was reinforced at 1500°C by solute hardening effects [13], and that strengthening of this phase occurred by formation of precipitates [5, 8, 15-18]. Yet, the development of the Nb-silicides is rather recent, and to define strategies aiming at improving the mechanical properties, proper identification of the elementary deformation mechanisms of the Nb_{ss} phase is necessary. To the best of our knowledge, this identification has not been undertaken so far.

Therefore, our aim here is to investigate the microscopic plasticity mechanisms occurring in the Nb_{ss} phase at 1000°C. Moreover, precipitation phenomena have also been investigated, to interpret the hardening phenomena of the Nb_{ss} phase reported in the literature [5, 8, 13, 15-18]. For this purpose, Nb-20Si-25Ti-6Al-3Cr-3Mo materials have been processed by a powder metallurgy route: ingot casting, gas atomization, and powder densification by spark plasma sintering (SPS). Then, samples have been submitted to interrupted compression tests under vacuum at 1000°C at a deformation rate of 10^{-4} s^{-1}, and the deformation sub-structures have been investigated by transmission electron microscopy (TEM). Because the preparation of TEM thin foils of composites made of brittle (Nb_5Si_3) and ducile (Nb_{ss}) phases is difficult, focused ion beam (FIB) methodologies have been employed.

2. Experimental

The nominal alloy composition chosen in this study was Nb-20Si-25Ti-6Al-3Cr-3Mo (all compositions are given in at.%). A rod was prepared using a water-cooled copper crucible in a furnace under argon atmosphere, with a 200 kW power supply. Elemental feedstock with purity higher than 99.5% (except for Si: 99.4%) was induction melted and cast to form the rod, 50 mm in diameter and about 400 mm in length. The rod was cleaned from any residue from the steel mold and argon-atomized in ONERA's crucible-free Electrode induction melting gas

atomization (EIGA) facility (ALD Vacuum Technologies, Germany). The [40-100] µm fraction was sieved out of the produced powder. Then, cylindrical samples 36 mm in diameter and 8 mm thick were processed by spark plasma sintering (SPS) from the sieved powder following usual procedures [19], using a Sumitomo 2080 equipment. The main parameters were the following. The heating rate was set to around 100°C/min from room temperature to 75°C below the targeted dwell temperature measured by a pyrometer (1450°C). Then, the heating rate was lowered to 25°C/min, to avoid excessive temperature overshoot due to the thermal inertia of the sample/die/punch assembly. The temperature was kept for 2 minutes before the heating current was turned off. Then, the graphite mold and the sample cooled down in the chamber. During the whole cycle, a uniaxial pressure of 50 MPa was applied to the sample, and the pressure in the SPS chamber was about 10 Pa. The temperature was measured on the external wall of the graphite die by an optical pyrometer, and the true sample temperature (which is used here) was determined from previous calibrations; for instance, for a 36 mm diameter sample, with the die thickness commonly used, the sample temperature is ca. 60°C higher than the temperature indicated by the pyrometer [20]. Taking also into account an observed overshoot of 40°C, the maximum sample temperature during the elaboration step of 2 minutes was thus of 1550°C ± 15°C.

From the cylindrical specimens, compression samples of 3×3×6 mm were cut by electrical discharge machining. Then, quasi-static compression experiments under vacuum at 1000°C under vacuum (5. 10^{-4} Pa before heating), and at a strain rate of 10^{-4} s^{-1}, have been performed on a Schenck testing machine of the ONERA laboratory using a furnace (Pyrox Thermique Matériaux, France) with Mo-based heating elements; the heating rate was 300°C/h. The total duration of the holding at 1000°C during the compression test was about 5 min. The samples were deformed by about 2 % of plastic deformation, a value that is suitable for post-mortem TEM investigations of the microscopic deformation mechanisms. As the sample are too small to use a strain gauge, only the cross-head displacement is used to monitor the strain; the elastic deformation of the grip assembly and the whole testing frame has thus to be taken into account. A first sample was deformed at more than 20% total plastic deformation and the total deformation needed to reach about 2% plastic deformation was determined and used for the subsequent compression tests (Fig. 1). The actual plastic deformations after the tests were checked by measuring the reduction in height of the specimens. Stresses in the range 570-580 MPa were reached at test end.

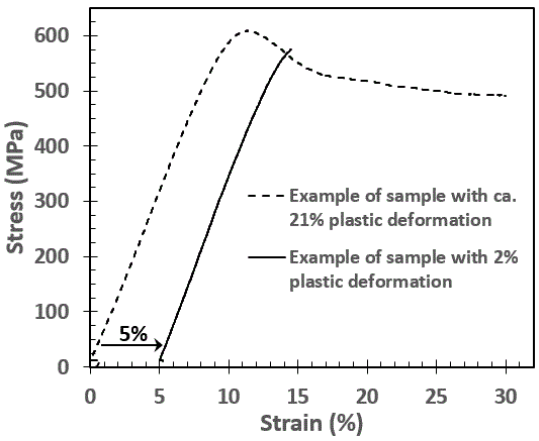

Fig. 1. Examples of compression curves for a first sample up to 22% plastic strain, and for a sample with a 2% plastic strain used for the investigations in the present work. The latter curve has been shifted by 5%.

For phase identification after elaboration, X-ray diffraction (XRD) was performed on the bulk specimens using a Bruker D8 Discover diffractometer equipped with a cobalt source (wavelength: 1.78886 Å) and 2D-detectors. Patterns were acquired from 20°-135° by 2θ steps of 0.005°, of which the 25°-90° portion is shown here for clarity. The crystal structure and the lattice parameters of the phases have been obtained by fitting the experimental patterns using the software PowderCell in a Rietveld-like analysis [22]. Since the patterns have been measured on bulk samples and not on powders, it is useless to apply more sophisticated softwares. The phase structure files (with space group, the atom Wyckoff positions, initial guess for the lattice parameters, etc.) are based on the phases in the binary system; a pseudo-Voigt peak profile has used, with a full width at half maximum (FWHM) represented by the usual Caglioti formula (parameters U, V and W) [23]. For the electron backscattered diffraction (EBSD) investigations, the sample were first metallographically prepared by polishing them with SiC papers and diamond suspensions, finishing with 2/3 of colloidal silica and 1/3 of 30% H_2O_2. Microstructure characterizations were performed by scanning electron microscopy (SEM) with an FEI Helios nanolab 600i equipment, in back-scattered electron (BSE) and energy-dispersive X-ray spectroscopy (EDS) modes. Thin foils for transmission electron microscopy (TEM) investigations were extracted by focused ion beam (FIB) using the same equipment, and employing procedures designed by Schaffer et al. [21] which have been adapted to our material. EBSD analyses were performed on this equipment with an Oxford detector, using a 20 kV acceleration voltage, and 11 nA beam current. TEM investigations of the plasticity mechanisms were performed with a 200 kV JEOL 2010 apparatus, using a tilt-rotation sample holder.

3. Results

3.1. Microstructure

Fig. 2-a shows the X-ray diffractogram of the material in the as-SPS state. In addition to the solid solution niobium phase (Nb_{ss}, bcc structure), other peaks are indexed as coming from the β–Nb_5Si_3 (tetragonal) and γ–Nb_5Si_3 (hexagonal) phases. The calculated peak positions and heights for the three phases have been added to Fig. 2a in form of "stick" patterns. The experimental and simulated diagrams (with the refined lattice parameters, scale factors, polynomial background parameters, FWHM parameters, etc.) overlap quite well. No preferred orientation is observed, as expected since the materials are made from particles with isotropic orientations. However, the intensities of the simulated diagrams do not match exactly the intensities of the experimental diagrams. Actually a simplified simulation has been used, e.g. with only Nb and Si atoms in the Nb solid solution and the various Nb_5Si_3 unit cells. Substituting partially Nb and Si by Ti, Mo, Cr and Al atoms in the cells affects the lattice parameters, which is taken into account in the fitting procedure, and also slightly the peak intensities depending on the hkl reflections. The latter has been neglected here, mainly because the distribution of the alloying elements on the possible Wyckoff positions is not well known in the complex Nb-Si alloys.

Fig. 2-b details the 40°-54° range where twenty-five reflections from the Nb_{ss} and α-, β- and γ-Nb_5Si_3 silicide phases overlap. The experimental diagram is well simulated when α-Nb_5Si_3 is not taken into account. The α-Nb_5Si_3 phase has not been identified by XRD, which means that either this phase has not been formed during the SPS processing route or its content is below the detection limit (about 1 volume percent). However, EBSD phase mapping has shown that this phase is present at a very low content in the as-SPS material, as shown in Fig. 3; it is mainly located in the β silicides, but also at Nb_{ss}/γ-Nb_5Si_3 interfaces and in the Nb_{ss} phase. The α-Nb_5Si_3 surface fraction measured on areas (~125 µm x 250 µm) larger than that presented in Fig. 3, is about 1%. Depending on the alloying elements and the processing conditions, the tP32-Nb_3Si silicide can be present in Nb-Si based materials. This phase has not been detected in the studied material, using XRD, EBSD, BSE imaging and EDS local chemical analysis.

The crystallographic data for the four phases are summarized in Table 1.

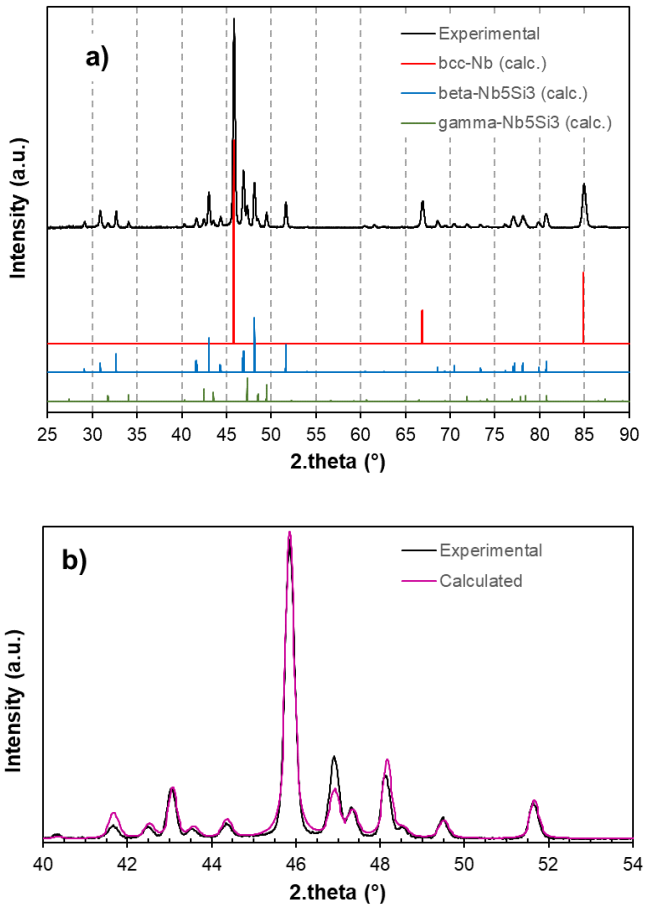

Fig. 2. (a) X-ray diffraction diagram in the as-SPS state. The calculated positions and peak heights for the Nb_{ss}, β–Nb_5Si_3 and γ–Nb_5Si_3 phases are shown as "sticks" to easily allocate an experimental peak to the adequate phase. (b) In 40°-54° range, comparison of experimental and simulated diagrams, the latter including only the Nb_{ss}, β–Nb_5Si_3 and γ–Nb_5Si_3 phases.

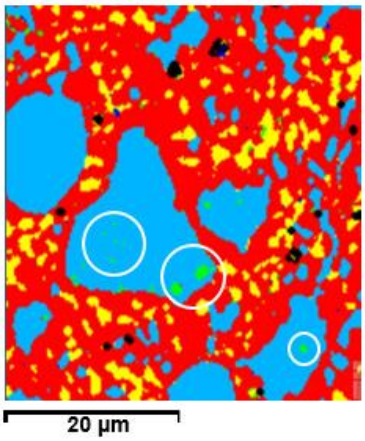

Fig. 3. EBSD phase mapping of the as-SPS material. Nb_{ss} (red), β–Nb_5Si_3 (blue), γ–Nb_5Si_3 (yellow). Small α–Nb_5Si_3 (green) is detected mainly in the β–Nb_5Si_3 bulky silicide.

Table 1. Phases present in the as-SPS state. The lattice parameters are taken from the results of the XRD pattern analysis in Fig. 2. The indicative area fraction of each phase are from EBSD analyses.

Phase name	Stucture type	Space group	Group #	Strukturbericht notation	Lattice parameters (nm)	Area fraction (%)
Nb_{ss}	W	$Im\bar{3}m$	229	A2	a = 0.32426	59
α-Nb_5Si_3	B_3Cr_5	$I4/mcm$	140	$D8_l$	Not detected by XRD	1
β-Nb_5Si_3	Si_3W_5	$I4/mcm$	140	$D8_m$	a = 1.00250 c = 0.50259	32
γ-Nb_5Si_3	Mn_5Si_3	$P6_3/mcm$	193	$D8_8$	a = 0.75250 c = 0.51780	8

Fig. 4 shows BSE micrographs of the alloy microstructure in the as-SPS state (Fig. 4a-b), and after compression at 1000°C (Fig. 4c-d). In the as-SPS state, the microstructure is composed of a niobium solid solution matrix Nb_{ss} containing primary β- and γ-Nb_5Si_3 silicides. Note that generally on BSE images, α- and β-Nb_5Si_3 silicides are difficult to distinguish because of a similar contrast: no information is retrieved here from the BSE images showing the presence of α-Nb_5Si_3. The microstructure is mostly unchanged after the compression tests at 1000°C.

The chemical composition of the phases are given in Table 2 and 3 for the as-SPS state and after testing at 1000°C, respectively. In the as-SPS state, the β-Nb_5Si_3 silicides exhibit both a light grey and a dark grey contrast. This is often observed in Nb-Ti-Si based alloys [16] and is due to segregation of Ti and other elements such as Al and Cr during solidification. The Ti content in β-Nb_5Si_3 and Ti-rich β-Nb_5Si_3 differ by about 4 at.%. In some Nb-Ti-Si alloys [16, 17], the Ti segregation leads also to a Nb_{ss} and a Ti-rich Nb_{ss} phase, the latter exhibiting a darker BSE contrast. This is not the case here. Actually, Nb_{ss} shows composition variation in Nb and Si with lower and upper values in the range 47-50 % for Nb and 2-9 % for Si, while the contents in Ti (27-28%), Al (7-8%), Cr (5-6%) and Mo (5-6%) are rather constant. The variation in Nb and Ti contents are thus small compared to cases where Nb_{ss} and a Ti-rich Nb_{ss} phases coexist, with the former about 10 at% richer in Nb and about 5% leaner in Ti than the latter: only one type of Nb_{ss} is observed in the studied alloy. The scatter in composition in the β-Nb_5Si_3 phases is low (±0.5%), whereas some variations are noticed in the γ-Nb_5Si_3 phases (35-37% Nb, 28-29% Ti, 27-29% Si, 4-5% Al, 1-2% Cr and 1-2% Mo).

After testing at 1000°C, the same main phases are present: Nb_{ss}, β-Nb_5Si_3, Ti-rich β-Nb_5Si_3 and γ-Nb_5Si_3. The compositions are close to that in the as-SPS state; the main evolution is the slight Si content reduction in Nb_{ss}. The composition of β-Nb_5Si_3 was not measured here, but data from other samples show that it is very similar than that in the as-SPS state.

However, at a finer scale, precipitates identified below as constituted of α-Ti solid solution (α-Ti_{ss}) and δ-$Nb_{11}Si_4$ phases, are observed in the Nb_{ss} phase, at the Nbss/β-Nb_5Si_3 interphase and at the grain boundaries. These observations show also that the α-Ti_{ss} precipitates are present both in the as-SPS state and in the state deformed at 1000°C. As the area analysed by EDS is larger than the dimension of the α-Ti_{ss} precipitates, the composition given in Table 3 takes into account the composition of the surrounding phases; however, it shows that the precipitates are enriched in Ti.

More accurate observations using the FIB and TEM techniques are shown in Fig. 5. They confirm that the δ-$Nb_{11}Si_4$ precipitates are present in the state deformed at 1000°C, but have not been detected in the TEM foils extracted from the as-SPS state.

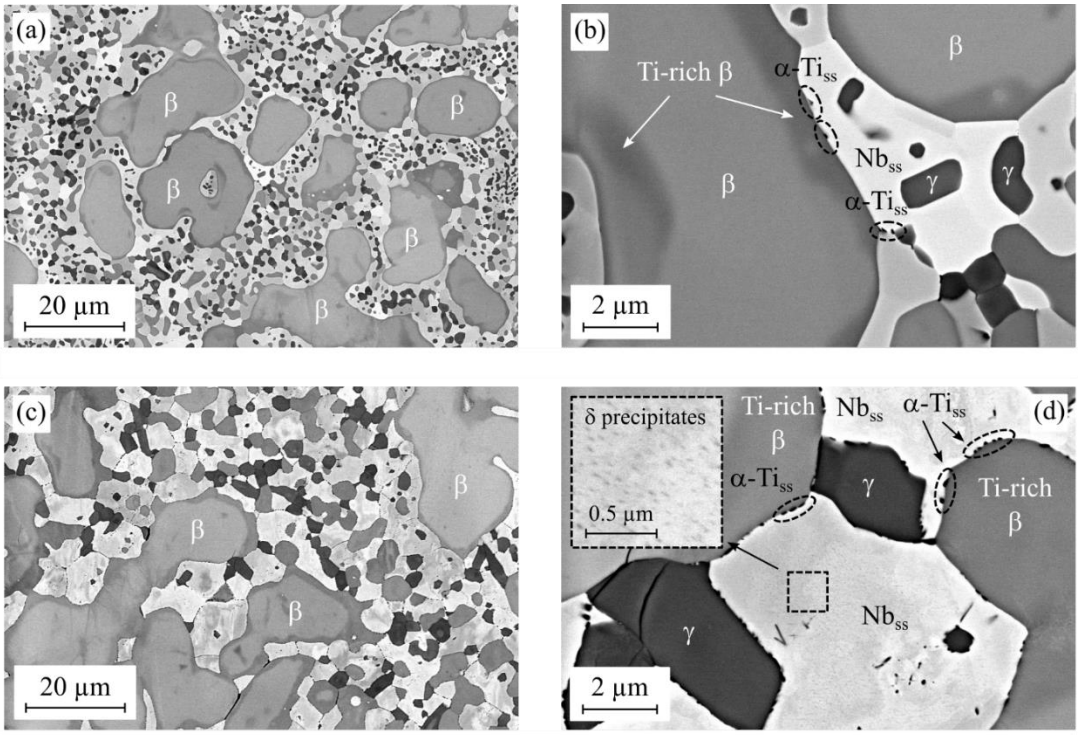

Fig. 4. BSE micrographs of the material in the as-SPS state (a-b), and after compression at 1000°C (c-d). In both states, the Nb_{ss}, β and γ phases appear in white, light grey and dark grey, respectively. Note in image (d), the presence of precipitates in the Nb_{ss} phase and at the interphase and grain boundaries, identified as constituted of α-Ti_{ss} and δ-$Nb_{11}Si_4$ phases.

Table 2. Mean composition (at.%) of the phases shown in Fig. 4a-b in as-SPS state

Phase		Nb	Ti	Si	Al	Cr	Mo
Nb_{ss}	white	49	28	4	8	5.5	5.5
β-Nb_5Si_3	light grey	45	17	32	3	1	2
Ti-rich β-Nb_5Si_3	dark grey	42	21	30	4	1	2
γ-Nb_5Si_3	black	36	29	27	4	2	2

Table 3. Mean composition (at.%) of the phases shown in Fig. 4d after test at 1000°C. Figures in parenthesis include the surrounding phases.

Phase		Nb	Ti	Si	Al	Cr	Mo
Nb_{ss}	white	51	27	2	8	6	6
β-Nb_5Si_3	light grey	-	-	-	-	-	-
(Ti-rich) β-Nb_5Si_3	dark grey	41	22	30	4	1	2
γ-Nb_5Si_3	black	38	28	26	4	2	2
α-Ti_{ss}	black	(41)	(36)	(9)	(6)	(4)	(4)

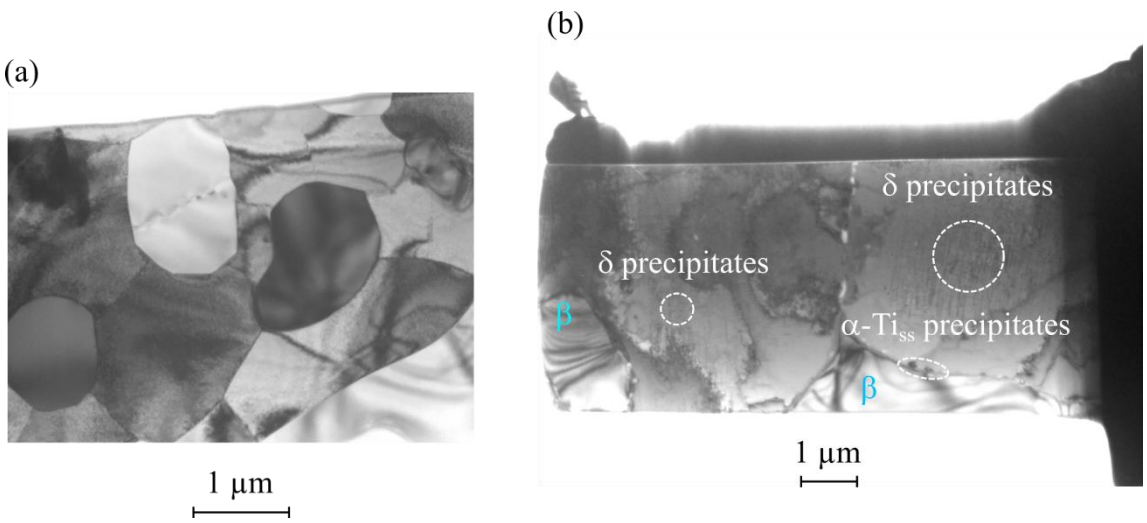

Fig. 5. TEM micrographs of FIB thin foils extracted in the as SPS state (a), and in the state deformed at 1000°C (b). Note in view (b) the presence of δ-$Nb_{11}Si_4$ precipitates, which are not seen in view (a). The very fine features which can be seen in view (a) are irradiation damages, which are known to occur in FIB extractions [24].

These precipitates have then been characterized in more detail. First, the precipitates at the interphase and grain boundaries have been identified, using selection area electron diffraction (SAED) techniques. The indexation of the diffraction patterns (not shown) have allowed to

identify the precipitates as being constituted of the low temperature "α" allotrope of titanium, hcp-Ti , in agreement with literature [3, 25], and to determine their crystallographic orientation. In the case presented in Fig. 6, the orientation of the α-Ti_{ss} precipitates and that of the G2 Nb_{ss} grain are given by the stereographic projections reported in Figs. 5 f and g, respectively. From these analyses, the following orientations relationships can be deduced:

$(0001)_{HCP\ Ti}$ // $\{110\}_{BCC\ Nb}$

$[11\bar{2}0]_{HCP\ Ti}$ // $<111>_{BCC\ Nb}$

Then, the very fine precipitates in the Nb_{ss} grains (Figs. 3d and 4b) have been identified by higher magnification TEM images (Fig. 7a). They exhibit an acicular morphology and are distributed in families perpendicular to each other. SAED experiments and dark-field images have been performed (Fig. 7b-d), which allowed to identify them as constituted of body-centered orthorhombic phase, by referring to previous works: such acicular precipitates were indeed determined as constituted of Nb_3Si [5], and, more recently, as δ-$Nb_{11}Si_4$ [8, 26]. Moreover, Fig. 7a shows that the precipitates are uniformly distributed in the Nb_{ss} grains, except near the grain boundaries, where zones depleted in precipitates over $\approx$ 1 µm width are observed. These two regions exhibit different deformation mechanisms, as will be discussed in the next section.

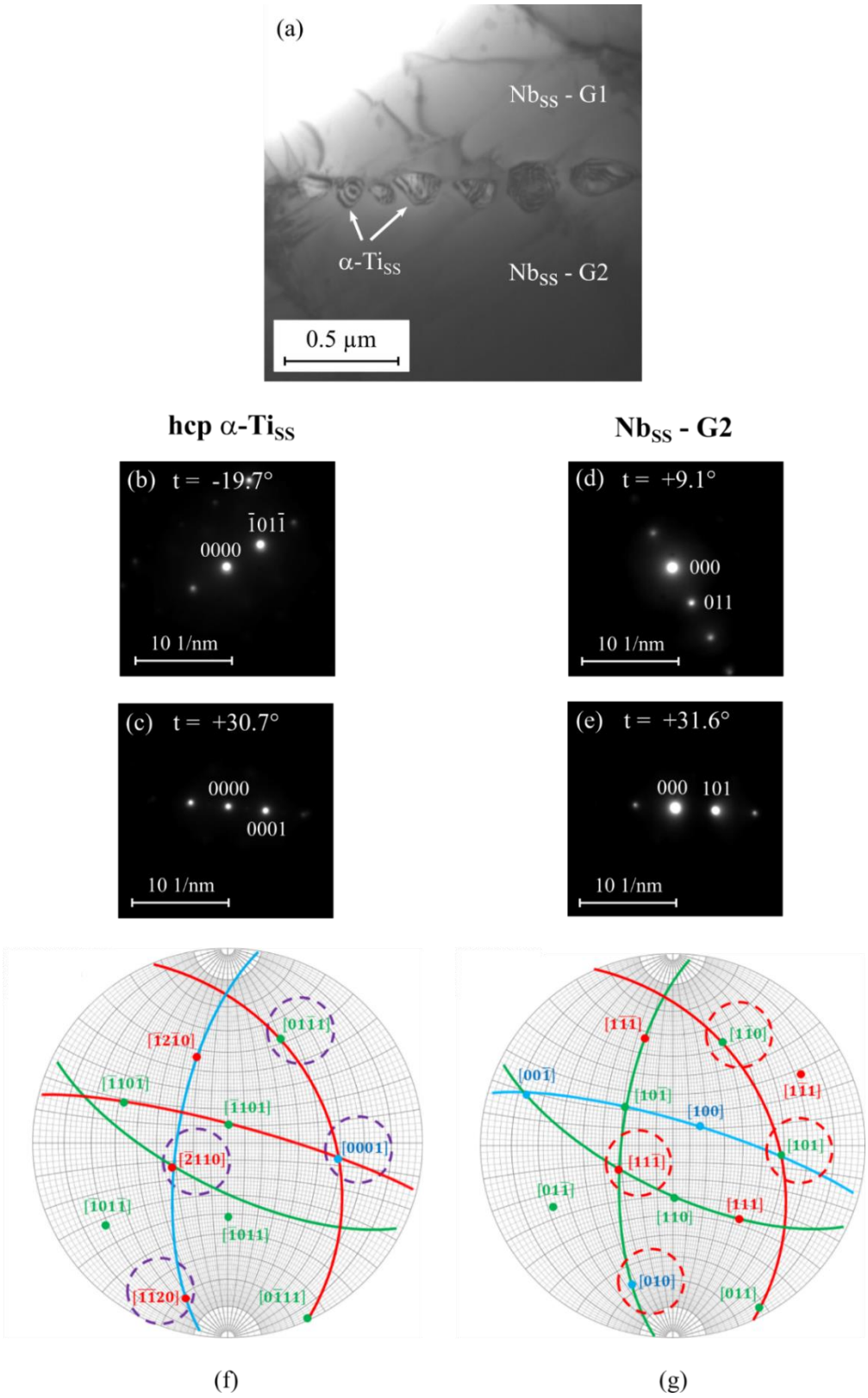

Fig. 6. (a) TEM micrograph of a FIB thin foil extracted at a boundary between two Nb_{ss} grains G1 and G2 (Nb_{SS}-G1 and Nb_{SS}-G2, respectively), in a sample deformed at 1000°C. (b-e) Examples of SAED patterns of the α-Ti_{ss} precipitates (left) and Nb_{SS}-G2 (right), with indication of the tilt angle t of the sample holder at which each pattern was obtained. (b-c) Stereographic projections of the α-Ti_{ss} precipitates and of the Nb_{ss} G2 grain, respectively, deduced from the above SAED investigations.

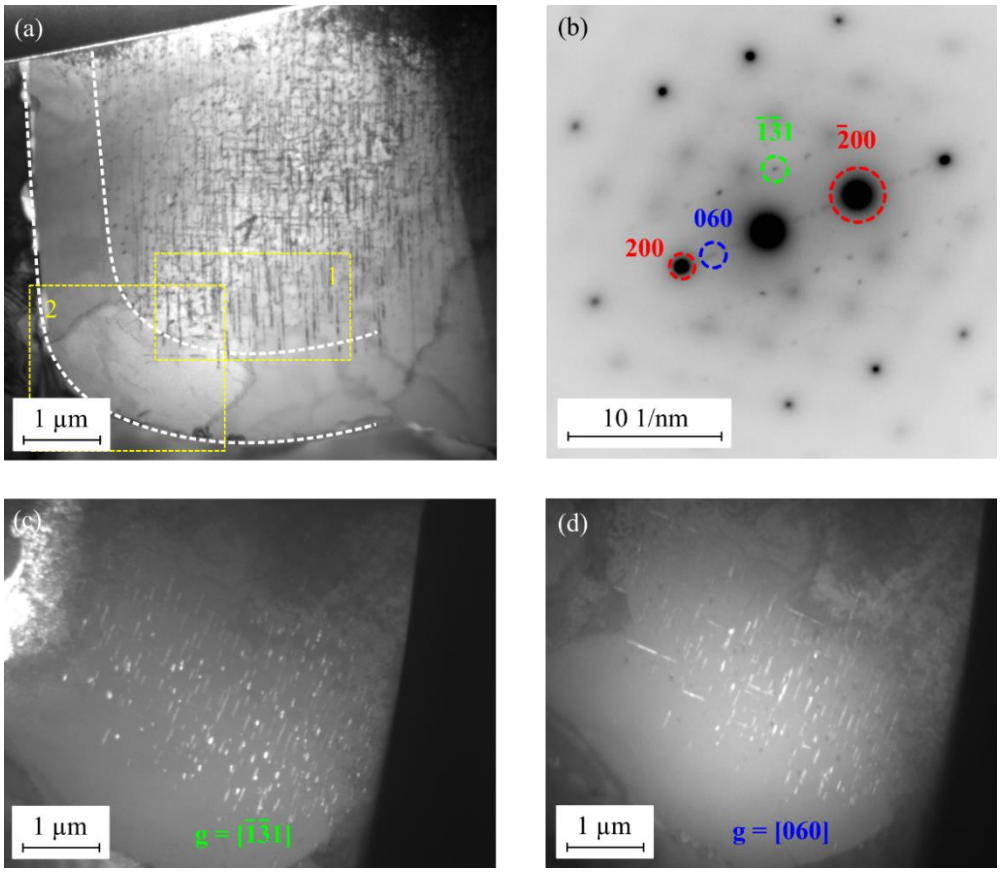

Fig. 7. (a) Bright-field TEM image of a Nb_{ss} grain in the deformed state at 1000°C. Note the presence of acicular precipitates in the interior of the grain, identified as constituted of δ-$Nb_{11}Si_4$ phase [5, 8, 26], and of a region depleted in precipitates in the vicinity of the grain boundary of the Nb_{ss} grain, delineated by white dotted lines. Inserts 1 and 2 have been more accurately investigated (see Fig. 9). (b) Two-beam SAED diffraction pattern of this grain in g = [200] condition (in red), showing fine spots belonging to two families of δ precipitates, δ_1 ($g = [\bar{1}\bar{3}1]$, in green) and δ_2 ($g = [060]$, in blue). (c) and (d): dark-field micrographs obtained by selecting the $\bar{1}\bar{3}1$ and 060 diffraction spots, respectively, showing the two families δ_1 and δ_1 of δ-$Nb_{11}Si_4$ precipitates.

3.2. Microscopic deformation mechanisms in compression at 1000°C

Fig. 8 shows a TEM thin foil extracted by FIB in a sample submitted to 2 % of plastic deformation at 1000°C. Diffraction analyses allowed to identify Nb_{ss}, β-Nb_5Si_3 and γ-Nb_5Si_3 regions, delineated in red, blue and yellow, respectively. It can be seen that many dislocations are present in the Nb_{ss} regions (Fig. 8b and c). On the contrary, the silicides (here, γ-Nb_5Si_3) appear as "clean", featureless regions (Fig. 8d). The same observation was made in β-Nb_5Si_3 silicides (see e.g. Fig. 5b). This shows that at 1000°C, the plastic deformation is only accommodated by the ductile Nb_{ss} grains, and that the brittle silicides remain undeformed.

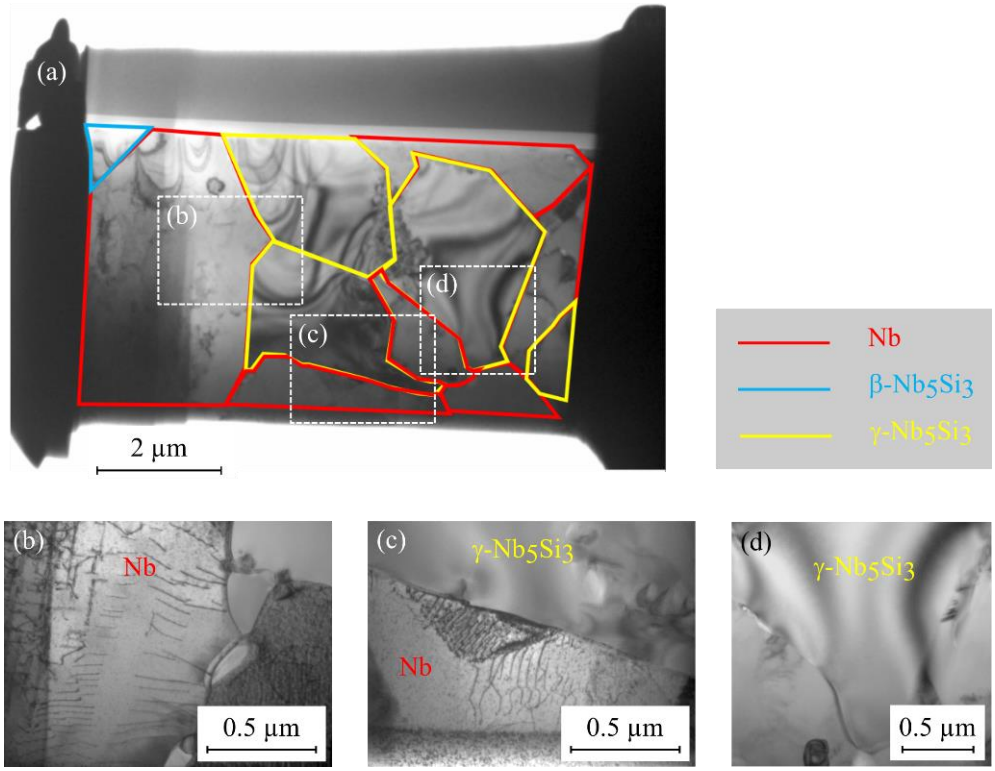

Fig. 8. TEM micrographs of a FIB thin foil extracted in a sample deformed in compression at 1000°C. (a) General view, on which Nb_{ss}, β-Nb_5Si_3 and γ-Nb_5Si_3 grains have been delineated. (b), (c) and (d): detailed views of Nb_{ss}, Nb-γ and γ regions, respectively. Note the presence of dislocations in the Nb region, and their absence in the γ-Nb_5Si_3 regions.

Hence, the observations have been concentrated in the Nb_{ss} grains, in which the deformation is concentrated. Fig. 9 shows detailed TEM images of the two inserts indicated in Fig. 7a. In Fig. 9a, taken in the interior of the Nb_{ss} grain, dislocations can be seen, which interact with the precipitates which are present in this zone. These interactions manifest themselves as pinning of the dislocation lines by the precipitates. Due to this phenomenon, the morphology of the dislocations was most of the time complex, and accurate identification of the elementary plasticity mechanisms, like glide or climb, was not possible. On the contrary, in the zones depleted in precipitates (Fig. 9b), the morphology of the dislocations was easier to investigate, due to the absence of pinning points. Rectilinear and curved dislocations could then be seen. Several diffraction analyses of dislocations located in such zones were performed, which made it possible to determine the Burgers vector $\vec{b}$ of different dislocation families using the extinction criterion $\vec{g} \cdot \vec{b} = 0$, where $\vec{g}$ is the diffraction vector. Burgers vector $\vec{b} = 1/2\,\langle 111 \rangle$ was thus determined, as it is usual in bcc structures [27]. Most of the time, the line of the dislocations was parallel to the Burgers vector, meaning a screw character. In this case, the deformation mechanism is straightforward: it is glide, because screw dislocation cannot climb.

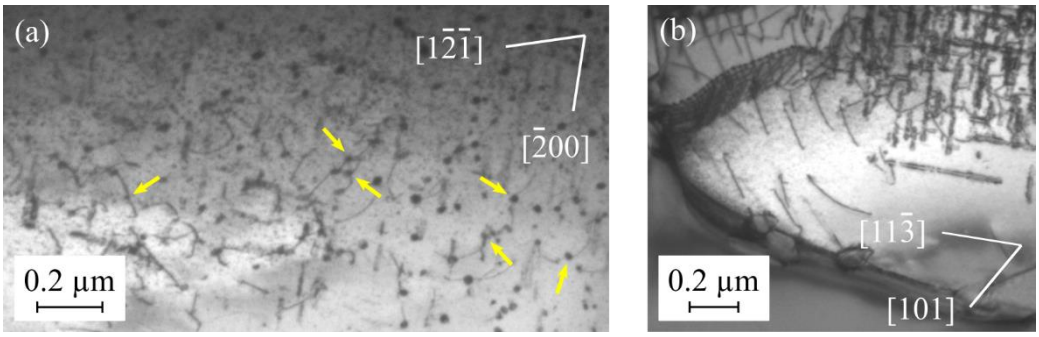

Fig. 9. Detailed TEM observations in the Nb_{ss} grain shown in Fig. 7a, inserts 1 and 2 (deformed state at 1000°C). (a) Insert 1: zone in the interior of the grain, containing δ-$Nb_{11}Si_4$ precipitates. Note interactions of the dislocations with the precipitates (some example of pinning points are arrowed). (b) Insert 2: zone at the periphery of the grain, depleted in precipitates. Note the presence of rectilinear and curved dislocations. The diffraction directions are indicated as solid lines.

However, because the deformation experiments were performed at high temperature (1000°C), it seemed natural to seek for a climb contribution. This required determining, for non-screw dislocations, the plane in which the dislocations move, which is then identified as glide or climb plane. To know whether the dislocations have moved by glide or climb, it is necessary first to determine their Burgers vector $\vec{b}$, and second their moving plane. If $\vec{b}$ is contained in the moving plane, then the mechanism is glide. If $\vec{b}$ makes an angle different from zero with the moving plane, then the dislocation motion includes a climb component. The determination of the Burgers vector is achieved by employing the classical $\vec{g} \cdot \vec{b} = 0$ extinction criterion. To determine the moving plane, curved dislocations have been investigated (which are of mixed character, that is, with non-screw segments), because in this case the curvature of the dislocation defines a plane, which is the plane in which the dislocation has moved [28]. Therefore, by observing a curved dislocation at different inclinations of the sample holder, it was possible to evaluate the orientation of the moving plane using geometrical reasoning. Fig. 10 shows an example of such determination. Fig. 10a shows a curved dislocation, which Burgers vector was previously determined as $\vec{b} = 1/2\,[\bar{1}11]$, under an inclination of the sample holder α of -45°. This image has been obtained by rotating the sample using a tilt-rotation sample holder, in order to put the two extremities of the loop parallel to the tilt axis, which corresponds to the vertical direction in the images. Then, when observed under α = -3° and α = +11°, this dislocation appears rectilinear. In other words, the dislocation is nearly edge-on in this angular range. Then, when α increases to +36°, the dislocation appears again as a loop. This means that, given the uncertainties of these measurements, the α angle for which the loop

plane is edge-on is 0° plus or minus about 10°. Furthermore, the trace of the loop plane is also vertical in the images, because its extremities were positioned parallel to the tilt axis of the sample holder, which corresponds to the vertical direction. This shows that the trace of the moving plane should correspond to the N-S vertical line in the stereographic projection (Fig. 10e), with an uncertainty of ± 10°. Consequently, the moving plane contains the Burgers vector $\vec{b} = 1/2\,[\bar{1}11]$, as shown by the stereographic projection, meaning that the mechanism is glide, and not climb.

However, the determination of the microscopic deformation phenomena in materials by TEM require in general investigations of tens of crystallographic grains, to determine the "average" dislocation mechanisms, from randomly observed dislocation morphologies. With samples prepared by the standard electropolishing techniques, large zones of tens of μm^2 can by observed, containing lot of crystallographic grains, from which many situations can be investigated. Here, electropolishing preparation techniques were attempted, but proved not suitable because of the very different thinning rates of the Nb_{ss} and silicide phases. Therefore, the samples had to be prepared by FIB, allowing observations on areas of ≈ 5×5 µm. Hence, only few crystallographic grains could be observed. This restricted considerably the opportunity to find dislocations suitably oriented for a proper identification of the mechanisms. Nevertheless, after preparation of 7 FIB thin foils, 4 were suitable for observation of deformation mechanisms, and each time the result was the same: the identified mechanism was glide, without evidence of climb.

4. Discussion

4.1. Precipitation in the Nb_{ss} phase

If the studied alloy, of composition Nb-20Si-25Ti-6Al-3Cr-3Mo, is supposed to be close to Nb-20Si-25Ti, its theoretical equilibrium microstructure can be evaluated using the Nb-Ti-Si ternary phase diagram drawn by Zhao *et al.* [6], based on an early determination of this phase diagram by Bewlay *et al.* [4]. Thus, according to the ternary phase diagram of Zhao *et al.*, at 1000°C, the composition Nb-20Si-25Ti is inside a hypothetical $(Nb,Ti)_5Si_3$-$(Nb,Ti)_3Si$-$(Nb,Ti)_{SS}$ three-phase domain, but very close to a $(Nb,Ti)_5Si_3$-$(Nb,Ti)_{SS}$ two-phase domain at 1000°C. The size of this two-phase domain increases at the expense of that of the three-phase domain when temperature decreases from 1200°C to 1000°C, meaning that the volume fraction

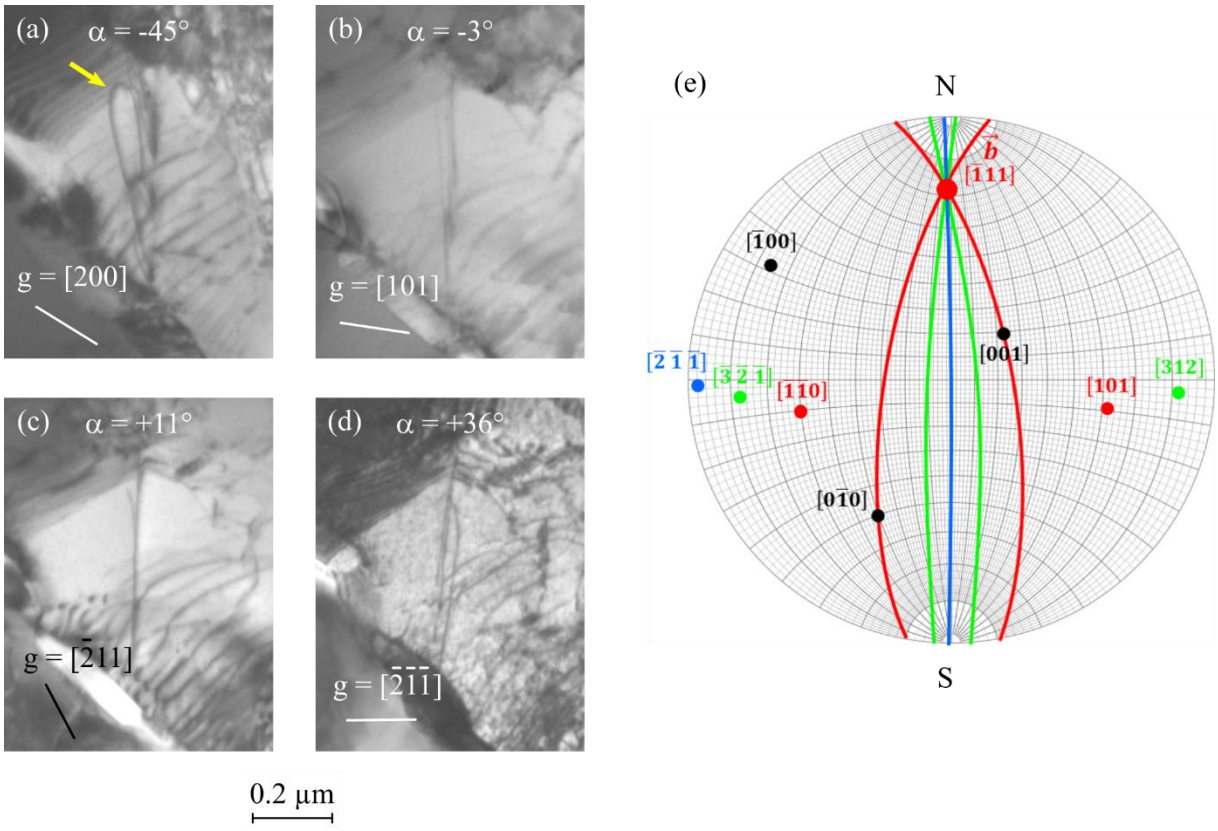

Fig. 10. (a-d) TEM bright-field images of a curved dislocation (arrow), for different inclinations α of the sample holder. Tilt axis is vertical in the images, and the corresponding diffraction directions are indicated (solid lines). (e) Stereographic projection of the Nb_{ss} grain for α = 0°, with possible moving planes represented in red, green and blue, with their respective poles.

of the $(Nb,Ti)_3Si$ phase tends to diminish with decreasing temperature. Then, conversely, when the temperature increases, formation of the $(Nb,Ti)_3Si$ phase is predicted to be promoted. If this phase corresponds actually more precisely to the δ-$Nb_{11}Si_4$ phase [8, 26], the formation of δ-$Nb_{11}Si_4$ precipitates during annealing at 1000°C could be accounted for by this interpretation, which assumes thermodynamic equilibrium. However, though these conclusions correspond to the experimental observations (Fig. 4d, Fig. 5b and Fig. 7), another interpretation is preferred. This phenomenon corresponds better to a classical precipitation phenomenon due to annealing of an (out of equilibrium) supersaturated Nb_{ss} solid solution. In the binary Nb-Si phase diagram, the solubility of Si in Nb is very low up to medium temperatures but reaches the maximum value of 3.5 at.% at the eutectic temperature (~1900°C) [6]. In the Nb-Ti system, the solubility of Ti in Nb is total above the hcp (α)/bcc (β) Ti transus temperature (~880°C), while the hcp and bcc phases coexist at lower temperatures. During the gas atomization step, the melt undergoes rapid solidification to yield fine particles. Diffusion phenomena have thus no time

to occur, which leads to particles with a Nb_{ss} phase supersaturated with Si and Ti. The powder is further compacted in short time, heated to 1550°C and quenched during the SPS cycle, at a rate slower than during atomization. The melting temperature of the material has been evaluated to be below or near 1600°C, by careful SPS experiments involving small amounts of powder: liquid matter is ejected out of the die at these temperatures. Actually, this defines a temperature at which the material's viscosity starts to be low enough to behave like a liquid under a small compressive stress, and is probably in the range of the temperature of the eutectic, and only a few tens of degrees higher than the SPS dwell temperature. The formation of δ-$Nb_{11}Si_4$ precipitates in the Nb_{ss} solid solution can thus occur through a precipitation mechanism from the supersaturated solid solution during the quenching of the material. A second opportunity for precipitation is during the compression test at a temperature indeed lower than the SPS dwell temperature, but for a longer duration because of the longer heating phase and the slower cooling rate related to the higher thermal inertia of the grip assembly.

The δ-$Nb_{11}Si_4$ precipitates have been studied in alloys manufactured in various systems, processing routes and thermal conditions. In [5], binary Nb-14Si and Nb-42Ti-15Si alloys were induction melted in a segmented water-cooled copper crucible and directionally solidified with a modified Czochralsky method. In [26], binary Nb-16/20/25Si alloys were arc-melted and studied in the as-cast condition, as in [15] for an Nb-10Si alloy. In [8], an Nb-22Ti-16Si-5Cr-3Al-3Hf alloy was arc-melted and heat-treated at 1450°C for 50 h. The precipitation of δ-$Nb_{11}Si_4$ can thus occur independently of imposed deformation. That δ-$Nb_{11}Si_4$ was not observed in the as-SPS state may be due either to the fact that favorable conditions for precipitation were not encountered before the thermal cycle for the compression test (relatively slow heating and cooling rates, dwell temperature of 1000°C), or to their absence in the investigated areas.

During cool down, the hcp α-Ti_{ss} phase can segregate from the bcc-Nb_{ss} solid solution: this is observed in Fig. 4 to 5, for instance at Nb_{ss}/β-Nb_5Si_3 phase boundaries (Fig. 4) and at Nb_{ss}/Nb_{ss} (Fig. 6) grain boundaries. Mao and Guo [3] have studied a Nb–22Ti–16Si–5Cr–5Al alloy and have also found hcp α-Ti_{ss} at Nb_{ss}/β-Nb_5Si_3 boundaries. They explain that this results from the diffusion of Ti from Nb_{ss} towards β-Nb_5Si_3 followed by the segregation of hcp α-Ti_{ss} at the interphase when β-Nb_5Si_3 becomes satured with Ti, which has led to the formation of a Ti-rich β-Nb_5Si_3 at the former Nb_{ss}/β-Nb_5Si_3 boundaries. Excess Ti in the Nbss solid solution is expelled and is trapped at the grain boundary if no adjacent phase is capable of incorporating this element; Ti can then diffuse along the grain boundary to segregate as an hcp α-Ti_{ss} phase.

This may be the case at Nb_{ss}/Nb_{ss} grain boundaries where the two grains exhibit comparable Ti contents.

Allen [7] suggests that elements in excess in Nb_5Si_3 can be ejected during heat treatments, and he specially considers Ti and Nb. Ti exhibiting a higher diffusion coefficient, is more likely to diffuse to the phase boundary and segregate as a Ti solid solution at Nb_5Si_3/Nb_5Si_3grain boundaries. These could also explain the presence of the α-Ti_{ss} phase (here with the hcp structure) at the Nb_{ss}/β-Nb_5Si_3 interphase, unless Ti diffuses to Nb_{ss}. However, Nb_{ss} already exhibits a higher Ti content than β-$Nb_5S\ i_3$, whether in as-cast or heat-treated state, and is able to form a Ti-rich Nb_{ss} phase [16,18].

Nb-Ti-Si based alloys exhibit macro-segregation in quenched conditions with numerous processing routes (liquid melt atomization, arc-melting, plasma-melting, cold hearth melting…), which can be mitigated or suppressed by heat treatments. The content in major elements as well as alloying elements shows thus spatial variations that affect the local out-of-equilibrium state (level of over-saturation etc.). Moreover, phenomena or features observed in one alloy can be affected by the presence or absence of one or more elements in another alloy, and synergistic effects can be encountered. All this makes the interpretation of fine phenomena difficult and would require more physical and thermochemical data (e.g. precipitation kinetics, solubility limits in phase diagrams, diffusion coefficients…).

4.2. Microscopic deformation mechanisms at 1000°C

The FIB preparation technique allowed observation of microscopic deformation mechanisms in some cases. However, as stated above, the difficulty of the technique, in the case of plasticity investigations, is that it allows only the observation of a few crystallographic grains. Here, 4 FIB thin foils have been investigated, in which the plasticity mechanisms could be identified in details.

It has been observed that the only phase which exhibits plastic deformation is Nb_{ss}. This is not surprising, because of the high deformability of metals at high temperatures. In the zones depleted in precipitates, where the dislocation morphology was not perturbed by pinning on δ-$Nb_{11}Si_4$ precipitates, the microscopic mechanisms have been investigated using stereographic approaches, an example of such investigation being shown in Fig. 10. It was found that the experimental moving plane contains the Burgers vector, meaning a glide mechanism. In case of climb, the moving plane would make a large angle with the Burgers vector. Then, consider

the potential moving plane roughly oriented vertically. In Nb, slip planes are reported as being {110} and {112}, but, more generally in BCC metals, slip in {123} is also reported when temperature increases, though more rarely [29]. Thus, the glide planes which orientations are compatible with that of the moving plane have been drawn in the stereographic projection (Fig. 10e). The $(\bar{2}\bar{1}\bar{1})$ plane appears to best correspond to the experimental glide plane. However, the two $(\bar{3}\bar{2}\bar{1})$ and (312) planes can also correspond. Finally, the two $(\bar{1}\bar{1}0)$ and (101) planes, which orientations seem too far from the vertical direction, can nevertheless be involved, through cross-slip from one plane to the other. Because the orientation of the $(\bar{2}\bar{1}\bar{1})$, $(\bar{3}\bar{2}\bar{1})$ and (312) planes are very close, and because of the limited accuracy of the tilting experiments, it is not possible to distinguish between these different possibilities. For the same reason, if cross-slip occurs between the two $(\bar{1}\bar{1}0)$ and (101) planes, leading to a mean orientation corresponding to that actually observed, it would not be possible to distinguish this cross-slip mechanism from glide in the $(\bar{2}\bar{1}\bar{1})$, $(\bar{3}\bar{2}\bar{1})$ and (312) planes.

In summary, glide has been observed in the 4 FIB thin foils (out of 7) which were suitable for plasticity studies. In these thin foils, climb was not evidenced. However, the deformation experiments have been carried out at 1273 K (1000°C), that is, at ≈ 0.46 times the melting temperature on Nb (2750 K). In metallic materials deformed in this temperature range, the dislocations moving by climb exhibit usually the tendency to re-arrange in sub-boundaries by recovery processes. Therefore, because most of the climbing dislocations are probably situated in these sub-boundaries, they are probably not any more visible in the microstructure. Sub-boundaries were also not detected, because the FIB procedure imposes too local investigations. Climb being controlled by diffusion, this phenomenon is slower than glide. Then, when the mechanisms of glide and climb coexist, the deformation kinetics is controlled by the latter. Consequently, though glide could only be evidenced here, climb is probably the rate-controlling phenomenon.

5. Conclusions

Nb-20Si-25Ti-6Al-3Cr-3Mo materials have been elaborated by SPS at 1550°C from a pre-alloyed powder. After elaboration, the microstructure was constituted of the following phases: Nb_{ss} (bcc structure), β-Nb_5Si_3 (tetragonal), γ-Nb_5Si_3 (hexagonal) and a small amount of α-Nb_5Si_3 (tetragonal); α-Ti_{ss} (hexagonal close packed) precipitates are located mostly at Nb_{ss}/β-Nb_5Si_3 grain boundaries. This material has been deformed in compression at 1000°C at a strain rate of 10^{-4} s^{-1} under vacuum, to investigate the microscopic plasticity mechanisms. Formation

of Si-rich precipitates has been observed after the compression tests, probably by precipitation phenomena driven by over-saturation of Nb_{ss} after elaboration at 1550°C. The Si precipitates, identified in literature as constituted of δ-$Nb_{11}Si_4$ phase, are distributed in the interior of the Nb_{ss} grains. Finally, glide of $\vec{b} = 1/2\langle 111 \rangle$ dislocations has been identified, but the mechanisms of glide in the possible {112} or {123} planes, or cross-slip in {110} planes, cannot be distinguished from each other. Climb could not be evidenced in these experiments, probably because of re-arrangement of the climbing dislocations in sub-boundaries. However, given the fact that the deformation occurred at 0.46 times the melting temperature on Nb, it is reasonable to assume that climb is the rate-controlling phenomenon. The dislocations interact with the precipitates, a phenomenon which potentially accounts for hardening phenomena of the Nb_{ss} phase.

Acknowledgements

The authors wish to thank the French ANR organization, through the project number ANR-15-CE08-0042, for funding. The SPS experiments have been performed on the Sumitomo 2080 machine of the PNF2-CNRS, Toulouse. This work has been supported by the French State under the "Investissements d'Avenir" program managed by ANR through the MATMECA project (reference ANR-10-EQPX-37).

References

[1] B.P. Bewlay, M.R. Jackson, P.R. Subramanian, J.C. Zhao. *A review of very-high temperature Nb-silicide-based composites*. Metall. Mater. Trans. A 34 (2003) 2043–2052.

[2] J.C. Zhao, J.H. Westbrook. *Ultrahigh-temperature materials for jet engines*. MRS Bull. 28 (2003) 622–630.

[3] W. Mao et X. Guo. *Effects of alloying and high-temperature heat treatment on the microstructure of Nb–Ti–Si based ultrahigh temperature alloys*. Prog. Nat. Sci. Mater. Int. 22 (2012) 139-145. doi: 10.1016/j.pnsc.2012.03.008.

[4] B.P. Bewlay, M.R. Jackson, H.A. Lipsitt. *The Nb-Ti-Si ternary phase diagram: evaluation of liquid-solid phase equilibria in Nb- and Ti-rich alloys*. J. Phase Equilib. 18 (1997) 264-278.

[5] R.J. Grylls, B.P. Bewlay, H.A. Lipsitt, H.L. Fraser. *Characterization of silicide precipitates in Nb–Si and Nb–Ti–Si alloys*. Philos. Mag. A 81 (2001) 1967-1978. doi: 10.1080/01418610108216647.

[6] J.C. Zhao, M.R. Jackson, L.A. Peluso. Map*ping of the Nb-Ti-Si phase diagram using diffusion multiples*. Mater. Sci. Eng. A 372 (2004) 21-27.

[7] A.J.S. Allen. *Phase Stabilisation of Nb-Si-Ti Alloys via Elemental Additions and Post-Processing*, PhD thesis, University of Leicester, 2019.

[8] X. Ma, X. Guo, M. Fu. *HRTEM observation of silicides and Laves phase precipitates in Nb-Ti-Si based alloys*. Int. J. Refract. Met. Hard Mater. 78 (2019) 138-145. doi: 10.1016/j.ijrmhm.2018.09.005.

[9] N. Sekido, Y. Kimura, S. Miura, Y. Mishima. *Solidification process and mechanical behavior of the Nb/Nb5Si3 two phase alloys in the Nb-Ti-Si system*. Mater. Trans. 45 (2004) 3264–3271.

[10] H.S. Guo, X.P. Guo. *Microstructure evolution and room temperature fracture toughness of an integrally directionally solidified Nb–Ti–Si based ultrahigh temperature alloy*. Scr. Mater. 64 (2011) 637–640.

[11] Z.P. Sun, X.D. Tian, X.P. Guo, M.J. Yin, F.Y. Zhang, X.M. Zhang. *Oxidation resistance and mechanical characterization of silicide coatings on the Nb-18Ti-14Si-9Al alloy*. Int. J. Refract. Met. Hard Mater. 69 (2017) 18–26.

[12] N. Wang, L.N. Jia, B. Kong, Y.L. Guo, H.R. Zhang, H. Zhang. *Eutectic evolution of directionally solidified Nb-Si based ultrahigh temperature alloys*. Int. J. Refract. Met. Hard Mater. 71 (2018) 273–279.

[13] W.Y. Kim, H. Tanaka, et S. Hanada. *Microstructure and high temperature strength at 1773 K of Nb_{ss}/Nb_5Si_3 composites alloyed with molybdenum*. Intermetallics 10 (2002) 625-634. doi: 10.1016/S0966-9795(02)00041-9.

[14] J.T. Guo, Y.X. Tian, G.M. Cheng, L.Z. Zhou, L.L. He, H.Q. Ye. *Microstructural characteristics and high temperature compressive properties at 1623K of a directionally solidified Nb-siliside based in-situ composite*. J. Alloys Compd. 470 (2009) 606.

[15] B. Cockeram, M. Saqib, R. Omlor, R. Srinivasan, L.E. Matson, I. Weiss. *Characterization of silicide precipitates in primary Nb phase in Nb-10%Si in-situ composites*. Scr. Metall. Mater. 25 (1991) 393–398.

[16] K. Zelenitsas, P. Tsakiropoulos. *Study of the role of Ta and Cr additions in the microstructure of Nb–Ti–Si–Al in situ composites*. Intermetallics 14 (2006), 639–659.

[17] K. Zelenitsas, P. Tsakiropoulos. *Study of the role of Al and Cr additions in the microstructure of Nb-Ti-Si in situ composites*. Intermetallics 13 (2005), 1079-1095.

[18] J. Geng, G. Shao, P. Tsakiropoulos. *Study of three-phase equilibrium in the Nb-rich corner of Nb-Si-Cr system*. Intermetallics 14 (2006) 832–837.

[19] J.P. Monchoux. *Sintering mechanisms of metals under electric currents. Spark plasma sintering of materials*, (P. Cavaliere Ed.), Springer, Cham, 2019. p. 93-115.

[20] T. Voisin, L. Durand, N. Karnatak, S. Le Gallet, M. Thomas, Y. Le Berre, J.F. Castagné, A. Couret. *Temperature control during spark plasma sintering and application to up-scaling and complex shaping*. J. Mater. Process. Technol. 213 (2013) 269-278.

[21] M. Schaffer, B. Schaffer, et Q. Ramasse. *Sample preparation for atomic-resolution STEM at low voltages by FIB*. Ultramicroscopy 114 (2012) 62-71. doi: 10.1016/j.ultramic.2012.01.005.

[22] W. Kraus and G. Nolze, *POWDER CELL-A Program for the Representation and Manipulation of Crystal Structure and Calculation of the Resulting X-Ray Powder Pattern*. J. Appl. Cryst. 29(3) (1996) 301-303. doi: 10.1107/S0021889895014920

[23] L.B. McCusker, R.B. Von Dreele, D.E. Cox, D. Louër and P. Scardi, *Rietveld refinement guidelines*. J. Appl. Cryst. 32 (1999) 36-50.

[24] Z. Trzaska, A. Couret, J.P. Monchoux. *Spark plasma sintering mechanisms at the necks between TiAl powder particles*. Acta Mater. 118 (2016) 100-108.

[25] X. Ma, X. Guo, M. Fu, Y. Qiao. *In-situ TEM observation of hcp-Ti to fcc-Ti phase transformation in Nb-Ti-Si based alloys*. Mater. Charact. 142 (2018) 332-339. doi: 10.1016/j.matchar.2018.05.052.

[26] G. Cheng, H. Qian, L. He, H. Ye. *Characterization of a new Nb–silicide (δ-$Nb_{11}Si_4$) in Nb–Si binary systems.* Philos. Mag. 90 (2010) 2557-2568. doi: 10.1080/14786431003630827.

[27] R.E. Smallman, A.H.W. Ngan. *Physical metallurgy and advanced materials*, 7th ed. Amsterdam ; Boston: Butterworth Heinemann, 2007.

[28] T. Voisin, J.P. Monchoux, M. Thomas, C. Deshayes, A. Couret. *Mechanical properties of the TiAl IRIS alloy*. Metall. Mater. Trans A47 (2016) 6097-6018.

[29] C.R. Weinberger, B.L. Boyce, and C.C. Battaile. *Slip planes in bcc transition metals*. Int. Mater. Rev. 58 (2013) 296-314. doi: 10.1179/1743280412Y.0000000015.